

Research Article

Seismic Behavior of T-Shaped Concrete-Filled Steel Tubular Column to Steel Beam Joints with Side Plates

Jinyan Wang ¹, Qinglu Li,¹ Yuzhou Sun,¹ Yi Zhao ¹, Zhonghao Niu,² and Xiaofen Li¹

¹School of Architecture and Civil Engineering, Zhongyuan University of Technology, Zhengzhou 450007, China

²Department of Civil and Environmental Engineering, Brunel University London, London UB8 3PH, UK

Correspondence should be addressed to Yi Zhao; 6357@zut.edu.cn

Received 16 June 2023; Revised 3 September 2023; Accepted 27 November 2023; Published 16 December 2023

Academic Editor: Gang Xu

Copyright © 2023 Jinyan Wang et al. This is an open access article distributed under the Creative Commons Attribution License, which permits unrestricted use, distribution, and reproduction in any medium, provided the original work is properly cited.

This study investigates the seismic behavior of the T-shaped concrete-filled steel tubular (CFST) column to steel beam joints, aimed at expanding their applicability in areas with high-seismic fortification intensity. A construction form of T-shaped CFST column to steel beam joint with side plates is presented. The variables studied in these experiments include the side plate length, the axial compression ratio, the presence of side plates, and the presence of binding bars. The force mechanism, failure modes, load–displacement curves, strength, stiffness, ductility, and energy dissipation capacity of seven specimens were evaluated under low-cycle reciprocating load. The experimental results demonstrate that the joints of side plates show a full hysteresis curve, with the ductility coefficient ranging from 1.67 to 2.49, and the equivalent viscous damping coefficient between 0.147 and 0.234. The joint panel zone displays strong deformation and energy dissipation capacity. The inclusion of side plates and binding bars improves the seismic behavior of the joint. The setting of side plates enables the formation of a plastic hinge on the steel beam, creating a beam hinge failure mechanism and satisfying the seismic design principle of “strong column and weak beam, strong joint and weak member” as required by the building structures.

1. Introduction

Special-shaped columns can eliminate indoor protruding column corners and improve indoor space utilization, while their torsional resistance decreases due to their irregular section compared with the rectangular columns. Consequently, there is a decrease in ductility and energy dissipation capabilities of special-shaped columns [1]. The application of special-shaped columns is thus restricted in practical engineering [2]. Special-shaped concrete-filled steel tubular (CFST) columns make best use of the advantages and bypass the disadvantages. The exterior steel tube has the restraint function to the concrete, and the interior concrete suppresses local buckling of the steel tube, providing high-bearing capacity and good deformation capacity [3, 4]. Additional measures, such as binding bars and vertical stiffeners, are also used to delay premature local buckling of steel tubes [5–8], further improving the constraining effect of steel tube on the core concrete. The special-shaped CFST column to steel beam joints plays a critical role as the transfer hub of the frame structural system.

These joints are subjected to a complex stress state under the combination of vertical and horizontal loads and are considered the weak point of the engineering structure against the seismic stress. Hence, it is crucial to develop a structure with clear force transmission, good seismic behavior, and convenient construction, which is the focus of promoting the special-shaped CFST column frame structure.

The existing studies primarily focus on the development of joints between steel beams and CFST columns with rectangular, circular, and square shapes [9–11], and few studies have assessed the seismic behavior of joints between special-shaped CFST columns and steel beams. The three commonly used joints are internal diaphragm joints, external diaphragm joints, and vertical stiffener joints. For internal diaphragm joints, Li et al. [12] conducted experimental and numerical study on the seismic behavior of internal diaphragm joints under the different loads. The results showed that the joint panel zone experienced shear damage while the beam end was fractured. Xue et al. [13] used the Park–Ang damage model to analyze the effects of various factors,

including axial compression ratio and concrete strength grade. The seismic behavior of spatial composite frame composed of special-shaped CFST column and steel beam with internal diaphragm connection was studied. Zhang et al. [14] analyzed the stress development process of L-shaped CFST columns based on the nonlinear analysis results. It is difficult to apply internal diaphragm connection to the special-shaped CFST column with small section because of the difficulty of welding construction and the disadvantage of concrete pouring. A study was investigated on external diaphragm connector, and the results showed that increasing the width of the external diaphragm can significantly enhance the load bearing capacity and energy dissipation capacity of the members [15]. Tang et al. [16] conducted an experimental study and theoretical analysis on two-story, two-span plane frame structures with special-shaped self-compacting CFST column to H-shaped steel beam external diaphragm joints. The result was that the frame structures showed good seismic performance. Zhang et al. [17] proposed a method to calculate the flexural load capacity of the joints with external diaphragm rings, considering different positions of the joints. The theoretical calculation results of the yield load and ultimate bending load were in satisfactory agreement with the experimental results. The external diaphragm joints are easy to construct and provide a reliable force transmission but they may pose challenges to the interior space arrangement due to the horizontal ring plate placed at the periphery of the CFST.

The vertical stiffener joint is a modified version of the external diaphragm joint, where the reinforcing ring plates located on both sides of the external diaphragm are replaced with the vertical stiffeners that are attached flat to the outside of the column, forming the vertical stiffener joint. Cheng et al. [18] and Xiong et al. [19] carried out the seismic behavior and shear capacity of joint specimens, utilizing various sizes and shapes of the vertical stiffeners. The experimental results revealed that the joints experienced plastic hinge damage at the beam end, and the researchers proposed optimal cross-sectional dimensions for the vertical stiffeners. The seismic behavior and the plastic hinge formation mechanism of special-shaped CFST column to steel beam frame structure with vertical stiffeners were analyzed by the experiment and finite-element method [20, 21]. Similar to the joints [21], Zhang et al. [22] proposed a cover-reinforced slotted side plate connection, and the results showed that the connection had positive effect on the progressive collapse resistance. The influence of external diaphragms and vertical stiffeners on seismic behavior of special-shaped CFST column to the steel beam joints were compared and calculated, Liu et al. [23] suggested that the vertical stiffener penetrate the joint panel zone, considering the shear damage in the external diaphragm joint panel zone, while the vertical stiffener joint failed to guarantee the plastic yielding of the steel beam. Different structural forms of special-shaped columns have different impacts on the seismic behavior of the joints. Cheng et al. [24] conducted the seismic performance of joints with external diaphragms and vertical stiffeners, using two types of the columns: multicell and binding bar. The experimental results demonstrated that vertical stiffener joints with

binding bars had the better seismic performance. Although the structure of vertical stiffener is simple, the vertical ribs are required to pass through the joint plate area for the special-shaped CFST columns with binding bars, otherwise brittle failure will occur.

There are a few other new types of joints. Li et al. [25] introduced a new joint connection method using U-shaped diaphragm plates to improve the plastic bending performance of the steel beams while satisfying the design code requirements in the United States, United Kingdom, and China. The diaphragm plate served as a joint to transfer the load from the beam to the joint panel zone. Zhao et al. [26] proposed the joint with side plates, and its flexural capacity was tested and simulated. Prefabricated built-in lattice type circular steel tube composite columns have been shown to have a good seismic behavior and economic benefits by investigating the damage mechanism of such structures [27]. Based on the previous research on the form and seismic performance of the special-shaped CFST column to steel beam joints, it is evident that the available types of such joints are limited.

According to the vertical stiffener joints, we propose a novel T-shaped CFST column to steel beam joints with side plates in this paper. The upper and bottom external rib plates are extended to form side plates lying flat in the joint panel zone. The reinforced side plates are welded around the exterior sides of the joint panel zone of the T-shaped CFST column and are further welded with the horizontal end plates and side plates. The side plates not only function as the backing plates for restraining the binding bars but also strengthen the confinement of the steel tube in the joint panel zone, improving the joint stiffness. This study aims to examine the seismic behavior of the T-shaped CFST column to steel beam joints under low-cycle reciprocating load. The investigated parameters include the side plate length, the axial compression ratio, the presence of side plates, and the presence of binding bars.

2. Experimental Procedures

2.1. Specimen Design. As shown in Figure 1, seven specimens with a ratio of 1:2 were designed. The parameters of the specimens are listed in Table 1. The T-shaped CFST column was constructed by welding a rectangular CFST column and a U-shaped steel tube, as illustrated in Figure 2. Subsequently, the T-shaped CFST column was welded to the prefabricated short steel beam, which was formed by welding horizontal end plates to a vertical end plate. The horizontal end plates were welded to the upper and lower flanges of the H-shaped steel beam using full-penetration welds, while the vertical end plate was connected to the web of the steel beam using splints and friction-type high-strength bolts. The width of the vertical end plate varied synchronously with the length of the horizontal end plate. Two 400 mm × 400 mm × 20 mm square plates were designed to cover the upper and lower ends of the CFST column to ensure better application of the axial loads during the tests. One end of the T-shaped hollow CFST column was welded and sealed with a square plate. The

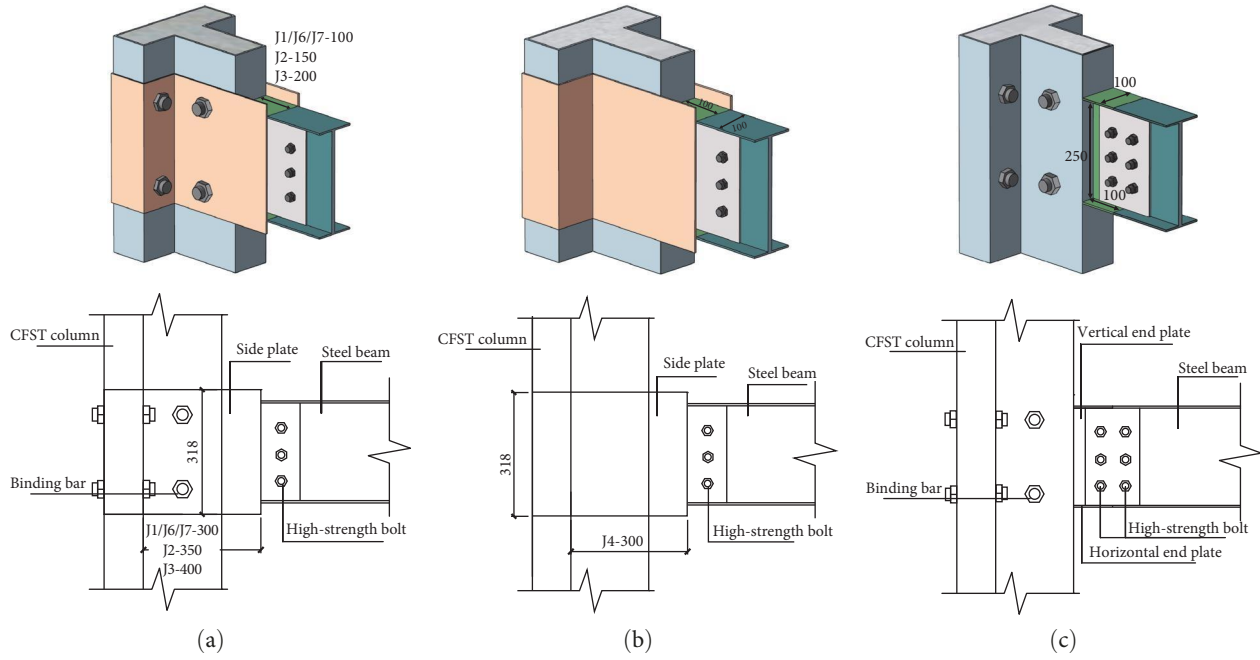


FIGURE 1: Details of the joints (unit: mm): (a) J-1, J-2, J-3, J-6, and J-7; (b) J-4; (c) J-5.

TABLE 1: The parameters of the specimens.

Specimen	Side plate (mm)	Horizontal end plate (mm)	Vertical end plate (mm)	<i>n</i>
J-1	300 × 318 × 4	100 × 100 × 4	250 × 100 × 4	0.2
J-2	350 × 318 × 4	100 × 150 × 4	250 × 150 × 4	0.2
J-3	400 × 318 × 4	100 × 200 × 4	250 × 200 × 4	0.2
J-4	300 × 318 × 4	100 × 100 × 4	250 × 100 × 4	0.2
J-5	–	100 × 100 × 4	250 × 100 × 4	0.2
J-6	300 × 318 × 4	100 × 100 × 4	250 × 100 × 4	0.4
J-7	300 × 318 × 4	100 × 100 × 4	250 × 100 × 4	0.6

section of the steel tube always remained flat during welding, and once the process was complete, the quality of the weld was examined. Qualified steel tubes were then filled with concrete, and the concrete pouring process was continuous and uniform. After pouring the concrete, the CFST columns were cured for 28 days. Then, the upper surface of the columns was polished and welded with another square plate. It should be noted that professional workers performed the welding, concrete pouring, installation, and fixation of all specimens. *N* is the axial compression ratio.

2.2. Material Properties. The steel used for the joints was Q235B, and the curing age of the concrete was 28 days. The mechanical properties of the selected steel and concrete were determined in accordance with the Chinese codes, GB/T 228.1-2010 [28] and GB/T 50,081-2019 [29], as presented in Tables 2 and 3.

2.3. Loading Method. This experiment investigated the seismic behavior of joint components subjected to low-cycle reciprocating load. According to the specification [30], a load–displacement hybrid control method was employed in

a quasi-static test in which the loading was applied to the column end, as shown in Figure 3. During testing, the specimens were subjected to the constant axial compressive loads imposed by a hydraulic jack and variable horizontal loads realized by an MTS electrohydraulic servo machine. The loading device is illustrated in Figure 4.

The specimens were subjected to preloading to eliminate any internal inhomogeneities, verify the experimental setup, and ensure the normal response of the measuring instruments. Three graded preloads were applied to the top of the columns with increments of 15% of the axial design load in each grade. The horizontal load was preloaded to a displacement of 1 mm per level, and the reciprocating cycle was loaded twice. In the formal loading stage, when the axial compressive load incrementally reached the design loading value, the horizontal load was imposed while the axial loading was maintained. When the horizontal load amounted to 60% of the estimated yield load, the loading amplitude was reduced, and each loading cycle was performed once. When the horizontal load reached the load at which the specimen yielded, the displacement control was used instead, and the

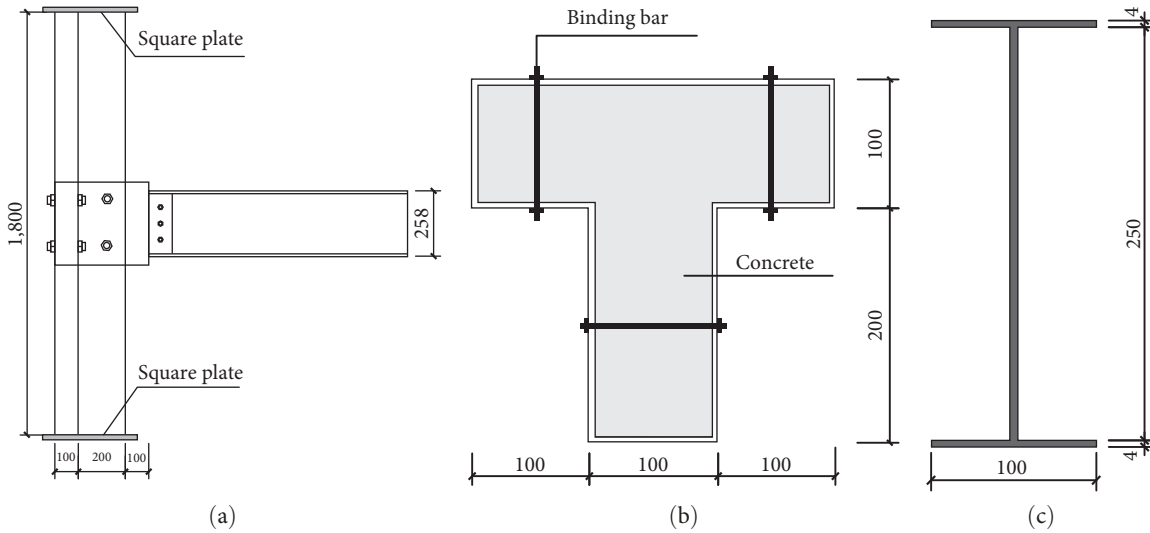


FIGURE 2: Details of the specimens (unit: mm): (a) overall specimens; (b) T-shaped CFST column; (c) steel beam.

TABLE 2: Material properties of steel.

Components	Thickness (mm)	Yield strength (MPa)	Tensile strength (MPa)	Elongation
T-shaped steel tube	5	324	447	0.21801
Steel beam/side plate	4	284	423	0.20437

TABLE 3: Material properties of concrete.

Concrete grade	Cubic compressive strength (MPa)	Axial compressive strength (MPa)	Elasticity modulus (MPa)
C40	43.4	33.2	3.21×10^4

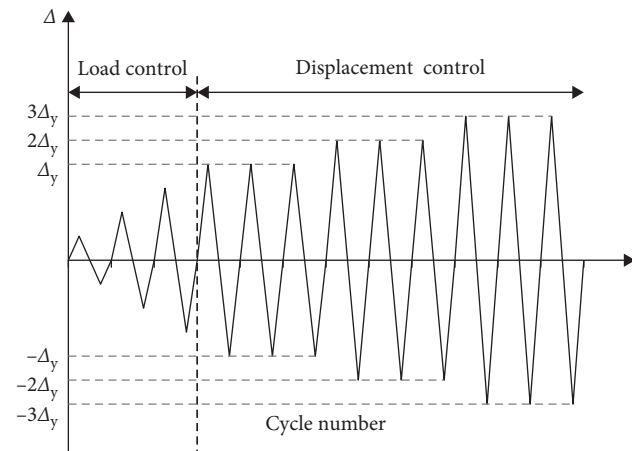


FIGURE 3: Loading scheme.

displacement value of each stage was taken as an integer multiple of the displacement value corresponding to the yielding moment. Loading based on incremental displacement was conducted three times, with a holding period of 10 min for each loading. The loading process stopped when the bearing capacity dropped to 85% of the peak load or the

specimen was significantly deformed. Deviation away from the reaction wall was deemed the positive loading direction, and direction toward the reaction wall was considered the negative loading direction.

2.4. *Distribution of Measurement Points.* Loads and horizontal displacements were measured and recorded during testing. Pressure transducers were set at column ends, and load data were automatically collected by a computer. Displacement gauges were arranged at column ends, column legs, beam ends, and relative corner areas of beams and columns to measure horizontal displacement at the column ends, displacement at beam ends, and deformation in the joint panel zone, including tensile displacement transducers LVDT2 and LVDT4, and thimble displacement transducers LVDT1, LVDT5, and LVDT7, as shown in Figure 5(a). The strain gauges were arranged symmetrically at the joint panel zone, the side plate, and the steel beam flange shown in Figure 5(b).

3. Results

3.1. *Test Phenomena.* Figure 6 illustrates the failure of benchmark specimen J-1. As the horizontal load reached 14 kN, the linear load–displacement curve of specimen J-1 changed to a nonlinear one, which indicated that specimen J-1 enters the

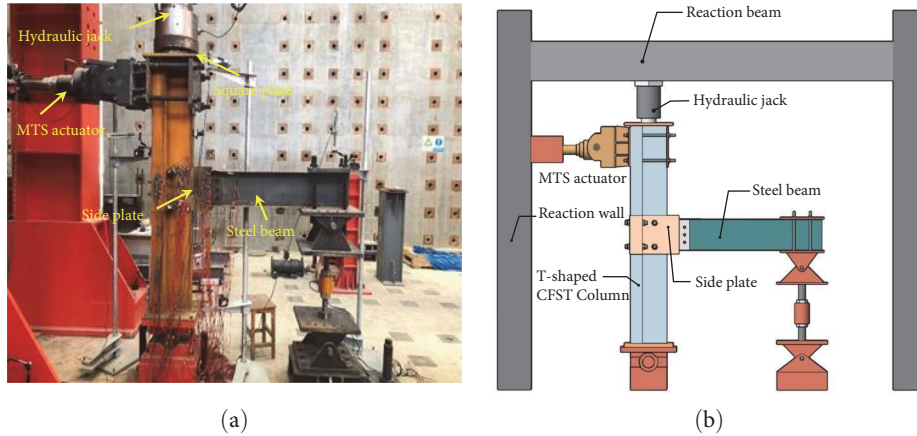


FIGURE 4: Loading device: (a) picture of loading device and (b) schematic diagram.

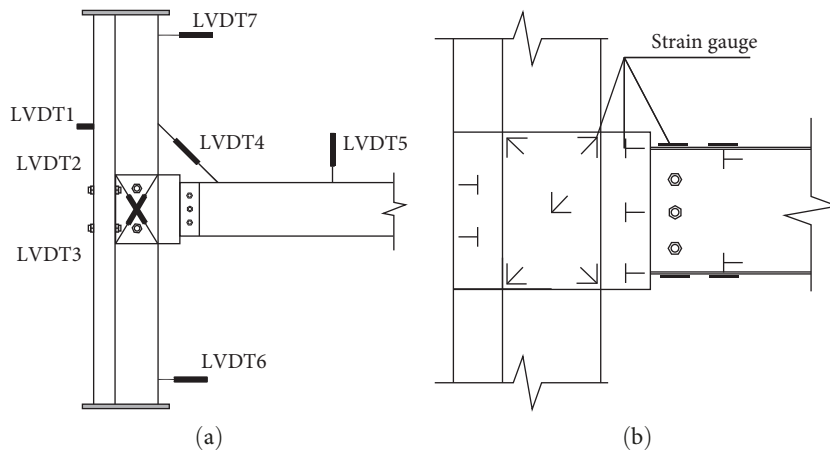


FIGURE 5: Measurement of specimens: (a) displacement gauges distribution and (b) strain gauges distribution.

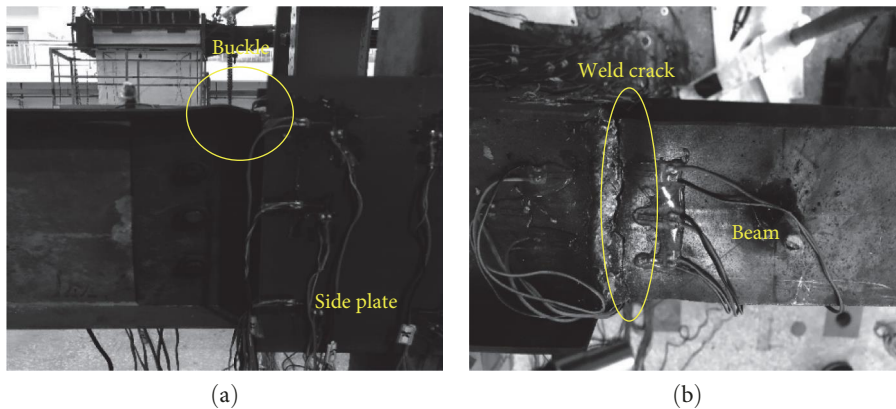


FIGURE 6: The failure of specimen J-1: (a) buckled and (b) weld crack.

elastic–plastic stage. At this time, the loading scheme was changed from load control to displacement control. As specimen J-1 was loaded to reach a positive displacement of 18.84 mm, the steel beams connected with the upper-end plates and side plates buckled. Raising the loading displacement and the action of reciprocating load increased the buckling degree of the upper

steel beam flange. Furthermore, fine cracks formed in the upper beam flange during the negative loading. As the negative displacement reached 18.89 mm, the upper flange failed by buckling and then the test was stopped.

Figure 7 shows the failure of specimen J-2. As the positive displacement reached 21.12 mm, the upper and lower flanges

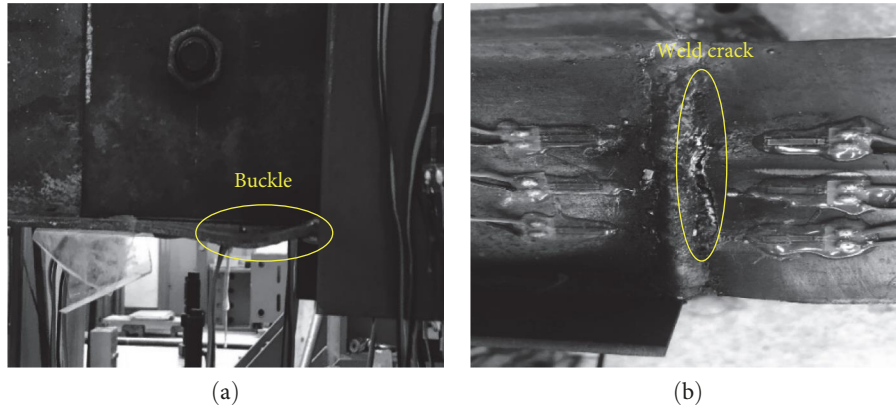


FIGURE 7: The failure of specimen J-2: (a) buckled and (b) weld crack.

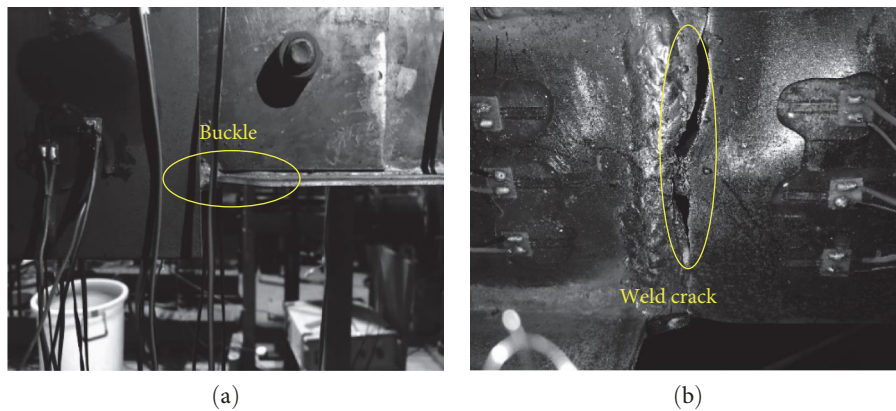


FIGURE 8: The failure of specimen J-3: (a) buckled and (b) weld crack.

of the steel beam connected with the side plates buckled and were then restored gradually in the unloading process. As specimen J-2 was loaded to reach a negative displacement of 26.4 mm, buckling failure occurred on the upper beam flange, and the cracks in the flange continued to enlarge and widen. The test was stopped when the upper beam flange fractured with a negative displacement of 31.68 mm. Meanwhile, the bearing capacity of specimen J-2 was reduced to 85% of the peak load.

Figure 8 depicts the failure of specimen J-3. When specimen J-3 was loaded to reach a negative displacement of 20.30 mm, buckling occurred on the lower beam flange connected with the side plates, while cracks formed in the upper flange. The buckling of the upper beam flange with a negative displacement of 26.1 mm was noticed. Finally, the upper beam flange fractured as the specimen J-3 was loaded to a negative displacement of 29 mm, while the remaining parts did not show apparent failure. The bearing capacity of specimen J-3 in the reverse displacement direction sharply declined to 85% of the peak load, and the test was then stopped. The failure patterns of the three components with different side plate lengths indicate that with the increase of side plate length, the buckling position of the steel beam flange developed from only the upper flange to both upper and lower flanges and then to the lower flange. Moreover, the

buckling failure all occurred at the upper flange of the steel beam.

Figure 9 shows the failure of specimen J-4 without binding bars. When it was loaded to reach a positive displacement of 17.4 mm, the upper beam flange connected with the side plates buckled; in contrast, at a negative displacement of 19.25 mm, local buckling was observed in the lower beam flange of the steel beam, and fine cracks formed in the upper flange. At the end of the first loading with a negative displacement of 30.8 mm, local fracture occurred on the upper beam flange of the steel beam; at the second loading, the test could not be continued because cracks penetrated the flange, and thus the loading was stopped.

Figure 10 shows the failure of specimen J-5 without side plates. When the horizontal load was higher than 12 kN, the deformation of specimen J-5 transitioned from the elastic stage to the plastic stage, with the loading method changing from load control to displacement control. The weld between the upper end plate and the column cracked in the first cyclic loading, with a negative displacement of 9.68 mm. The horizontal weld between the lower end plate and the column cracked when the positive displacement of specimen J-5 in the third cyclic loading reached 29.04 mm. After the third cycle, the vertical weld between the upper and lower end plates and the column cracked as specimen J-5 was loaded

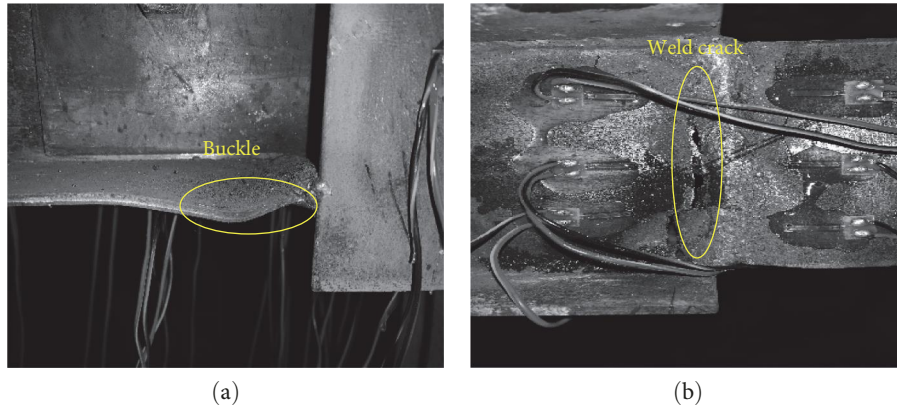


FIGURE 9: The failure of specimen J-4: (a) buckled and (b) weld crack.

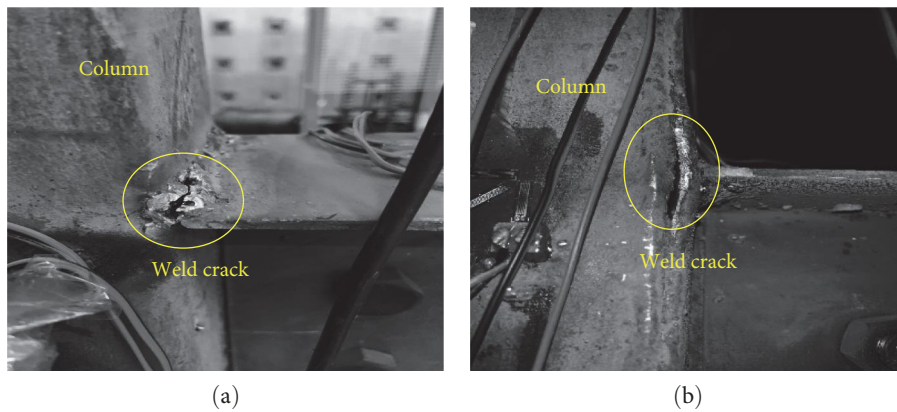


FIGURE 10: The failure of specimen J-5: (a) horizontal weld crack and (b) vertical weld crack.

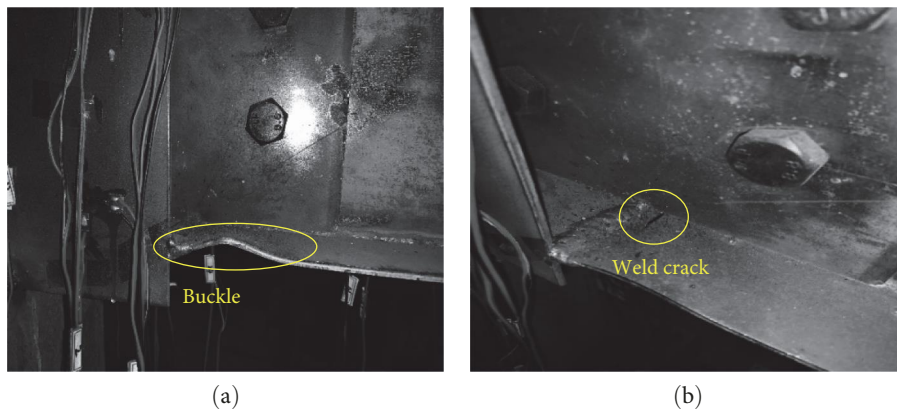


FIGURE 11: The failure of specimen J-6: (a) buckled and (b) weld crack.

to reach a positive displacement of 33.88 mm. At this time, the joint panel zone reached the plastic state, and the loading was stopped.

Figure 11 depicts the failure of specimen J-6 with an axial compression ratio of 0.4. When specimen J-6 was loaded to reach a positive displacement of 8.8 mm, fine cracks formed in the weld between both the upper and lower end plates and the steel beam. When it was loaded to reach a negative

displacement of 11 mm, the cracks penetrated the weld between the upper end plate and the steel beam, and the lower beam flange buckled. In the first cyclic loading with a positive displacement of 24.2 mm, the connection between the lower beam flange and the lower end plate experienced a tearing failure. In the third cyclic loading, the lower beam flange fractured, the bearing capacity of the specimen plummeted to 85% of the peak load, and the loading was stopped.

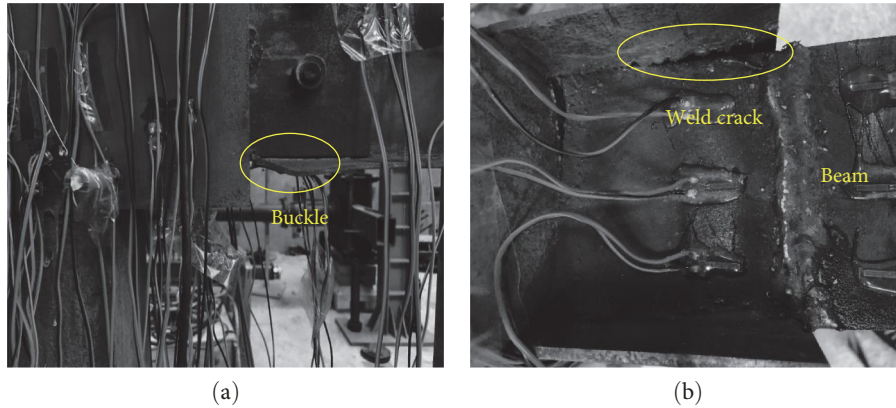


FIGURE 12: The failure of specimen J-7: (a) buckled and (b) weld crack.

Figure 12 depicts the failure of specimen J-7 with an axial compression ratio of 0.6. The weld between the horizontal end plate and the vertical side plate cracked when specimen J-7 as loaded to reach a positive displacement of 17.08 mm. The lower beam flange also buckled as it was loaded to reach a negative displacement of 17.08 mm. The weld between the horizontal end plate and the vertical side plate formed a large crack at a positive displacement of 29.89 mm. The loading was stopped because specimen J-7 was significantly damaged, although its bearing capacity remained stable within a specific range and did not continue to decrease.

3.2. Failure Modes. Specimens J-1, J-2, J-3, J-4, J-6, and J-7, which were all joints with side plates, experienced a “beam–hinge failure”. For specimens J-1, J-2, J-3, and J-6, the load on the column end was transferred to the steel beams through the side plates. The bending moment and shear force were carried by the flange and web of the steel beam respectively. The joint panel zone demonstrated excellent load transfer capacity as the side plates and short beams combined to form a box section. Throughout the test, with the increase of applied load, no obvious deformation occurred in the joint panel zone and T-shaped CFST column, and the ultimate local buckling failure occurred in the steel beam flange. The maximum strain of the joint panel zone was $216 \mu\epsilon$, the maximum strain of the side plate was $879 \mu\epsilon$, while the strain of the steel beam flange exceeded the yield strain of steel ($1,120 \mu\epsilon$). It demonstrated that other components except steel beam were in the elastic stage, indicating that the joints had a distinct force transmission path with reasonable stress. The joints failed on the connection between the side plates and beam flanges, which was regarded as a beam–hinge failure, complying with the seismic design principle of “strong column and weak beam, strong joint and weak member.” The lack of binding bars in specimen J-4 compacted the concrete casting in the column, resulting in a more significant displacement, and internal force withstood when the failure occurred. In fact, its bearing capacity did not improve, but it delayed the failure of the steel beam. The bearing capacity of specimen J-7 improved due to an axial compression ratio of 0.6, which also caused a change in the failure phenomenon. To account for the initial defects and residual stresses in the welds between the side plate and the

CFST column, as well as the upper end plate joint, the external load in the elastic phase was distributed based on the beam–column linear stiffness ratio. This prevented any deformation of the specimen itself. However, as the reciprocating load increased, the weld between the horizontal end plate and the CFST column as well as the side plate became damaged. The internal force on specimen J-7 was redistributed, which eventually led to the cracking of its weld.

Specimen J-5, T-shaped CFST column to steel beam joint without side plates, underwent a column–hinge failure. The plastic deformation of the CFST column increased consecutively as the reciprocating tension and compression enlarged. Under the synergistic action of the load at the end of the column, the bending moment of the beam ends, and shear force, the joint panel zone underwent a plastic hinge, leading to the crack in the joint panel zone. The bearing capacity of specimen J-4 did not increase with the enlargement of the external load. The failure occurring in the joint panel zone can be considered a shear failure since the stiffness of the column was higher than the stiffness of the steel beam, it bore more bending moment and load under the action of external load. In the plastic stage, most of the external load was imposed on the column, which resulted in the failure of the column first and the column–hinge failure later. The above results demonstrate that joints with side plates offer good seismic behavior.

4. Discussion

4.1. Hysteresis Curves. Figure 13 shows the displacement–load relationship of the seven joint specimens. The hysteresis curves of the six joints with side plates show full shuttle shapes. The joints of such specimens exhibited linear hysteresis loops during the initial loading stage, but as the member yielded, the area of the hysteresis loop moderately enlarged. Furthermore, throughout the loading, the area of the hysteresis loop was basically unchanged as the amount of cycles was raised under the same displacement, indicating that the joints experienced no significant stiffness degradation. The area of the hysteresis loop expanded and gradually inclined to the displacement axis with the increase in the displacement, which implies that the stiffness of the joints degrades to a certain degree in the process of energy absorption because the

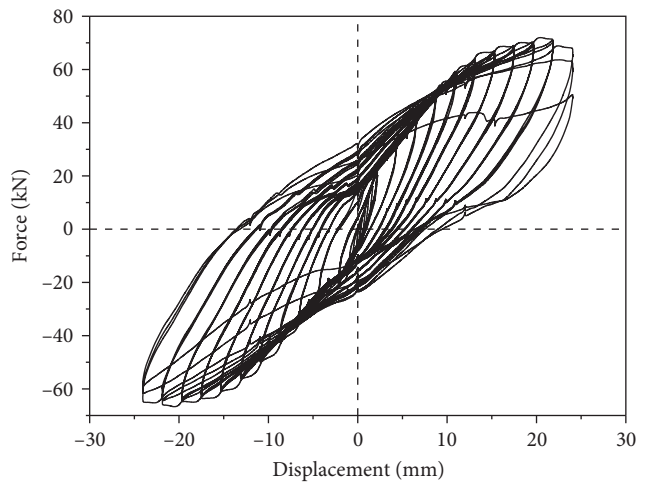
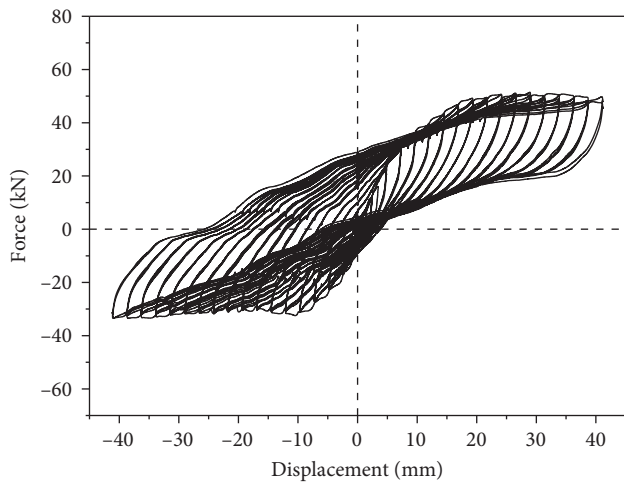
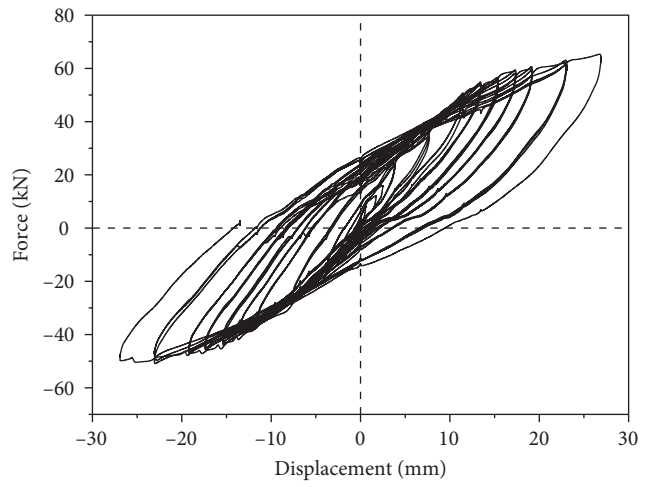
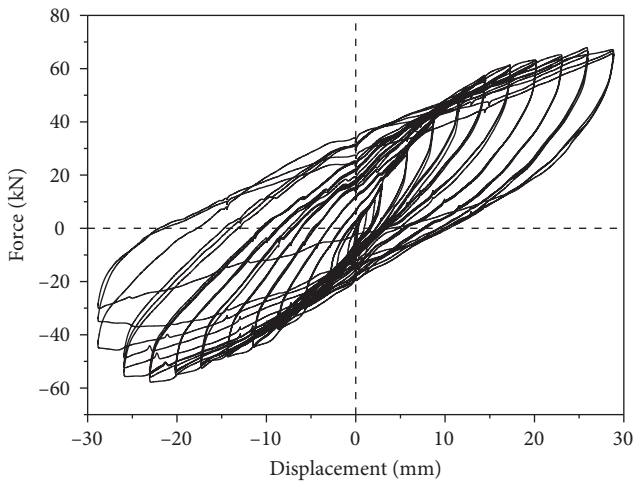
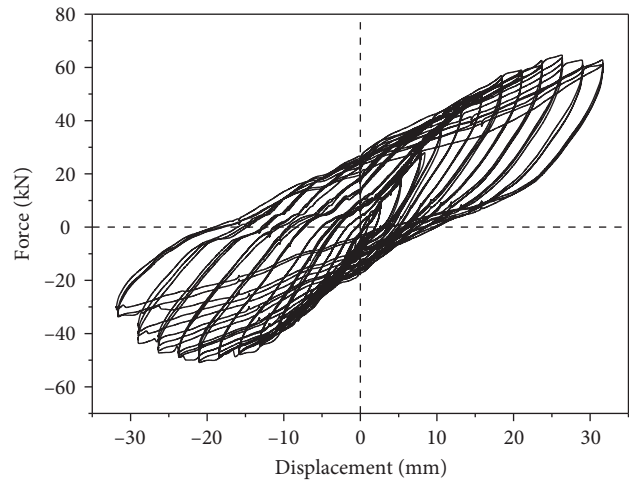
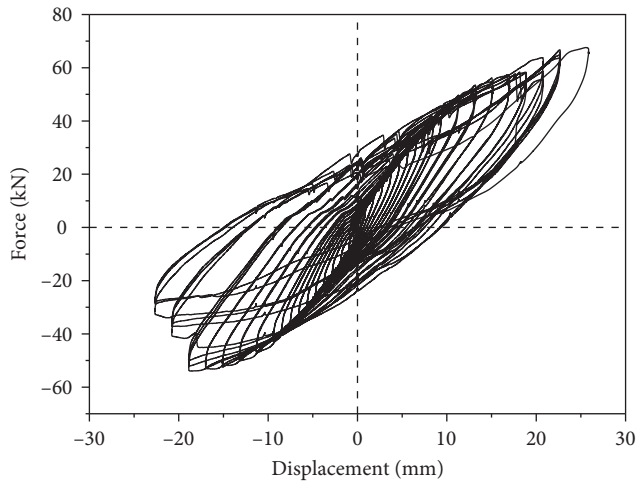


FIGURE 13: Continued.

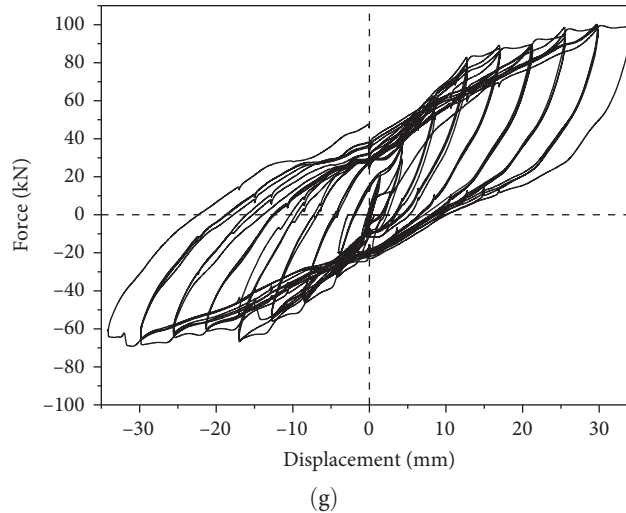


FIGURE 13: Hysteresis curves: (a) J-1, (b) J-2, (c) J-3, (d) J-4, (e) J-5, (f) J-6, and (g) J-7.

upper and lower beam flanges undergo local buckling and crack under the horizontal load. The cracks penetrated the steel beam as the load increased until local failure occurred, and the damage to the specimen intensified. As can be seen from Figure 13(e), the hysteresis curve of specimen J-5 exhibited a significantly different behavior compared to the other specimens, as it took an inverse Z-shape. Furthermore, the failure mode of specimen J-5 was also different from the other specimens, as the ultimate load drop was not significant when the specimen was ultimately damaged by the load. Furthermore, specimen J-5 lacked the constraint imposed by the side plates, leading to a low capacity to transmit the energy generated by the external load to the steel beam. Therefore, the energy could only be dissipated in the panel zone, resulting in the appearance of the plastic hinge in the panel zone and weld tearing on the joint, which is in line with the column–hinge failure mode. Different from specimen J-5, the other specimens were constrained by the side plates, so the plastic hinge was formed at the end of the beam. Under external loading, the energy that should be consumed by the panel zone was absorbed by the plastic hinge at the beam end through the bending deformation to heighten the energy dissipation capacity of the joints with side plates.

4.2. Skeleton Curves. Figure 14 delineates the skeleton curves of the specimens influenced by the different factors. The positive and negative skeleton curves of the joints are asymmetrical, and the load dropped quickly when the joints were loaded in a negative direction. The ultimate bearing capacity of specimen J-5 without side plates significantly decreased compared to that of specimen J-1 with side plates. The bearing capacity of the specimens seldom improved significantly with the length of side plates stretched from 300 to 400 mm. Specimen J-1 was the first to reach the ultimate load during loading and was more likely to experience strength degradation, and it was less plastic than specimen J-2 and specimen J-3. Specimen J-4 without binding bars was plastic slightly, nevertheless, the binding bars could not vastly improve the ultimate bearing capacity. The higher the axial compression

ratio was, the higher the bearing capacity was. The peak load of specimens J-6 and J-7 in the positive direction increased by 5% and 42%, respectively, compared to the specimen J-1.

All the joints with side plates underwent four stages during loading: elasticity, elastoplasticity, plasticity, and failure. At the beginning of loading, the skeleton curves grew linearly, indicating that the specimens were in elasticity. As the load increased, the curves began to show nonlinear changes. The steel beam flanges experienced local buckling deformation and formed fine cracks, implying that the specimens were in elastoplasticity. The cracks gradually expanded and deepened until the specimens yielded, and then the joints entered the plastic stage with internal force being redistributed. At this time, the growing speed of the bearing capacity declined, and the bearing capacity held steady for a short period after reaching the peak load. When the loading continued, the cracks in the flanges continued to enlarge until the failure finally occurred. Subsequently, the joints failed as the bearing capacity of the specimens declined sharply.

4.3. Ductility. The ductility coefficient (μ) is used to evaluate the deformation capacity of the specimens, which is expressed by Formula (1) and listed in Table 4:

$$\mu = \frac{\Delta_u}{\Delta_y}. \quad (1)$$

The yield load (P_y) and yield displacement (Δ_y) of the specimens can be determined by the yield moment method [24, 31], which is given in Figure 15. The detail of the drawing can be found in [32]. The load and displacement corresponding to the peak point of the skeleton curve are the peak load (P_m) and peak displacement (Δ_m), and the ultimate load (P_u) and ultimate displacement (Δ_u) refer to the value when the load drops to 85% of the peak load. Since some specimens did not reach the ultimate state at the end of testing, P_u and Δ_u were replaced by the value obtained at the end [24, 33] and marked with an asterisk (*) in Table 4.

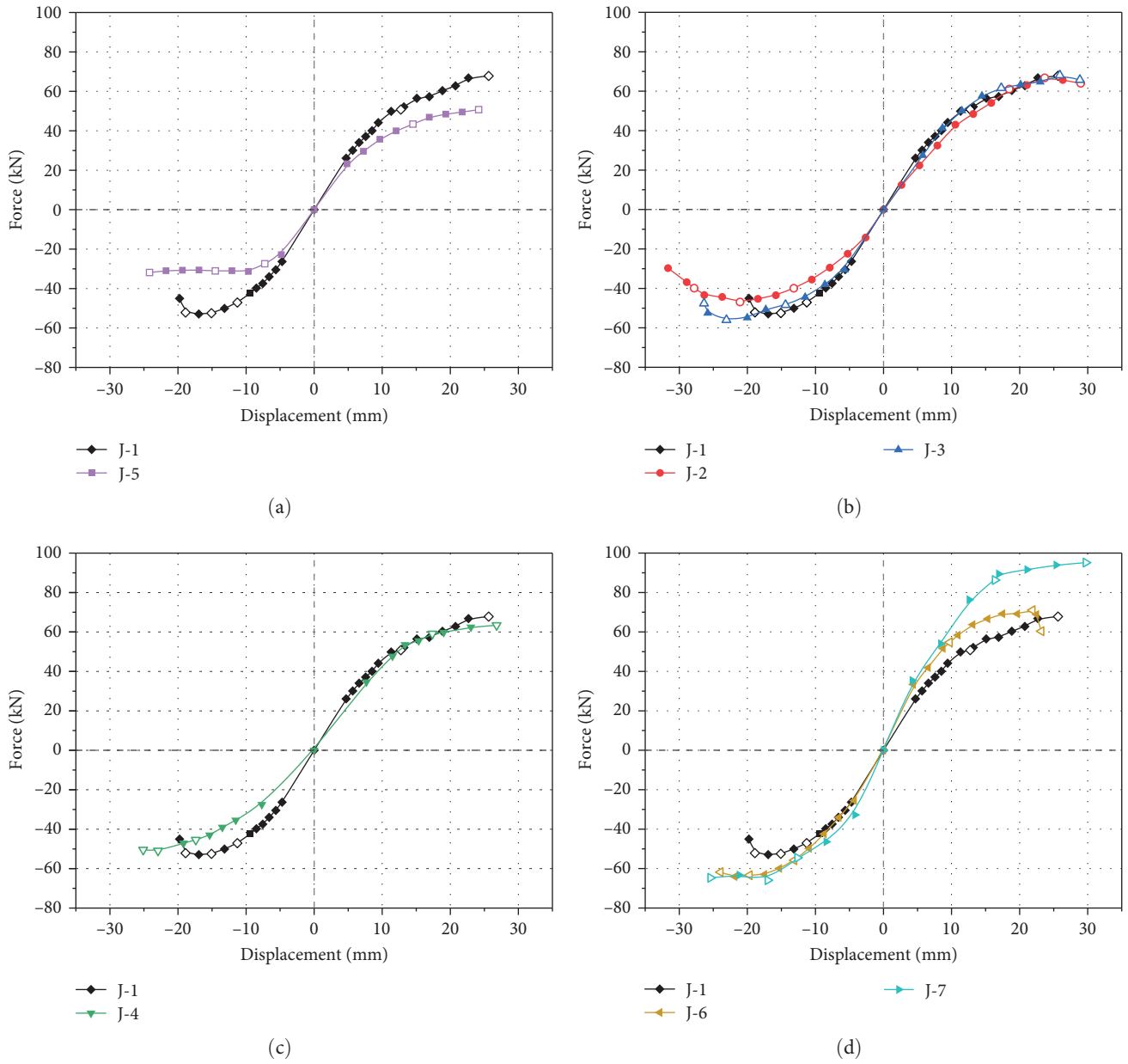


FIGURE 14: The skeleton curves: (a) side plates, (b) different the length of side plates, (c) binding bars, and (d) different the axial compression ratio.

TABLE 4: Loads and displacements of characteristic points.

Specimen	P_y (kN)	Δ_y (mm)	θ_y (rad)	P_m (kN)	Δ_m (mm)	P_u (kN)	Δ_u (mm)	θ_u (rad)	μ
J-1	47.84	11.87	1/152	52.98	16.94	45.03	19.77	1/91	1.67
J-2	39.56	13.11	1/137	46.91	21.09	39.87	27.82	1/65	2.12
J-3	48.40	14.25	1/126	55.98	23.07	47.58	26.37	1/68	1.85
J-4	45.64	17.83	1/101	50.94	22.93	50.48*	25.11*	1/72	1.41
J-5	28.48	8.04	1/224	31.32	9.66	30.95*	21.76*	1/83	2.71
J-6	54.69	9.71	1/185	71.05	21.87	60.39	23.17	1/78	2.39
J-7	53.75	11.93	1/151	65.91	17.05	64.40*	29.65*	1/60	2.49

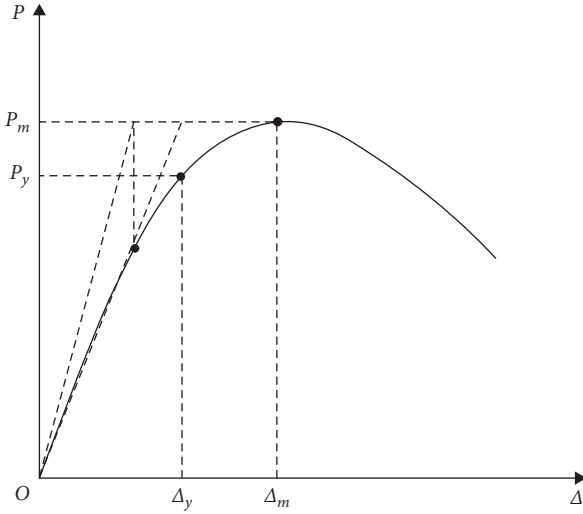


FIGURE 15: The yield moment method.

Five specimens (excluding J-4 and J-5) offered good seismic behavior with a displacement ductility coefficient ranging from 1.67 to 2.49 and averaging 2.10. Specimen J-4 without binding bars had the lowest displacement ductility coefficient among the seven specimens, indicating that the combination of the side plate and binding bars could enhance the ductility to some degree. Although specimen J-5 without side plates had the largest displacement ductility coefficient, plastic hinges formed in its joint panel zone, causing a column–hinge failure. According to the China’s relevant standards [34], the elastic interstory drift limit (θ_e) of multistory rectangular CFST frames is $1/300$, i.e., $\theta_e = 1/300$, and their elastic–plastic interstory drift limit (θ_p) is $1/50$, i.e., $\theta_p = 1/50$. Table 4 demonstrates that the elastic interstory drifts (θ_y) are all higher than θ_e , and the elastic–plastic interstory drifts (θ_u) are all close to θ_p , indicating that the specimens had better deformation capacity in the yielding and failure stages. The specimens with a larger length of side plates and axial compression ratio had better ductility.

4.4. Stiffness Degradation. The secant stiffness (K_i) is used to investigate the stiffness degradation trend [30], as expressed in Formula (2):

$$K_i = \frac{|+F_i| + |-F_i|}{|+X_i| + |-X_i|}, \quad (2)$$

where F_i and X_i are, respectively, the load and displacement corresponding to the highest point of the load–displacement curve at each loading grade.

K_i of the specimens followed a gradual degradation trend with the loading displacement, according to the stiffness degradation curves shown in Figure 16. The steel and concrete functioned independently without noticeable synergy in the initial loading stage, resulting in a high-stiffness degradation rate. As the displacement load progressed, the interaction between the members was enhanced, leading to a slower stiffness degradation. Specifically, after the steel

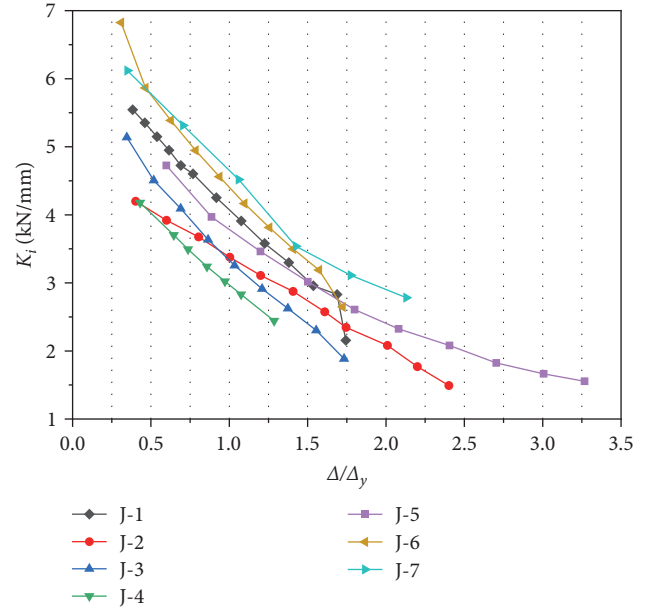


FIGURE 16: The stiffness degradation curves of the specimens.

beam buckled, the internal forces were redistributed, resulting in joint external loads being shared by both the beam and column. The stiffness degradation rate and initial stiffness of the specimens J-6 and J-7 were the largest, and their secant stiffness was higher than that of the specimen J-1, implying remarkable degradation. It is possible that the second-order effects of gravity (the P – Δ effect) is more significant with the increase of axial compression, and the additional bending moment becomes more and more obvious influence on the internal structural force with the increase of displacement, aggravating the accumulated damage to the specimens after yielding. Specimen J-4 without binding bars had the lowest secant stiffness, indicating that binding bars can improve the stiffness of the joints. The secant stiffness of specimen J-5 without side plates was lower than that of specimen J-1, implying that side plates can enhance the stiffness of the joints. As the length of side plates stretched, the secant stiffness of specimens J-2 and J-3 at each loading grade was lower than that of the specimen J-1, indicating that the excessive length of side plates cannot enhance the stiffness of the joints and delay the stiffness degradation.

4.5. Strength Degradation. This part calculates the strength degradation in the displacement control phase. As an essential indicator of measuring the seismic behavior of joints, the strength degradation coefficient (λ_i) reflects the cumulative damage to the joints. Equation (3) defines the strength degradation coefficient as follows:

$$\lambda_i = \frac{F_j^2}{F_j^1}, \quad (3)$$

where F_j^2 and F_j^1 are the load values corresponding to the peak points of the load–displacement curve at the second and first cycles of the j th loading, respectively.

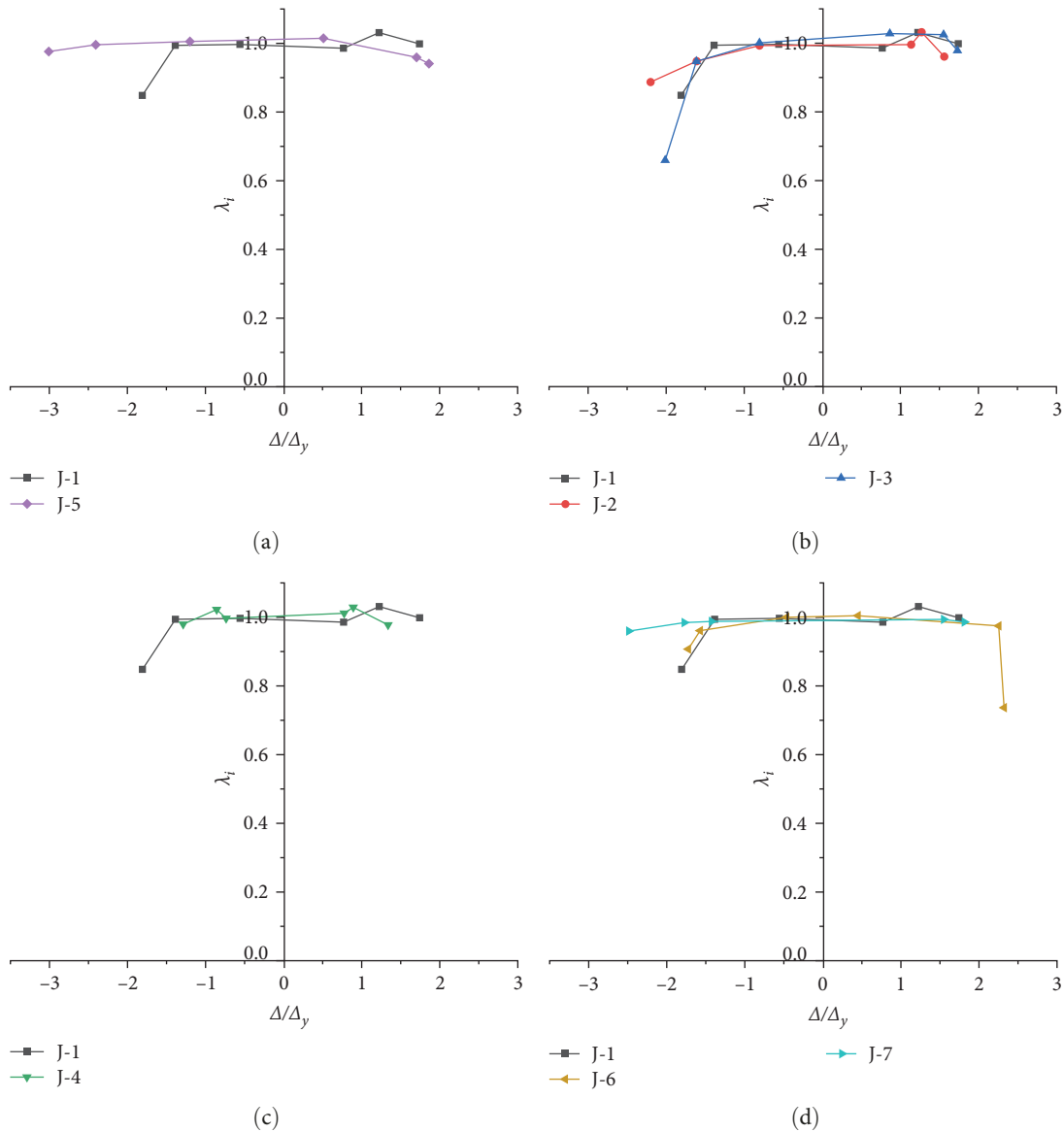


FIGURE 17: The strength degradation curves: (a) side plates, (b) different the length of side plates, (c) binding bars, and (d) different the axial compression ratio.

Figure 17 delineates the relationship between λ_i and Δ/Δ_y of the specimens affected by various factors, where Δ stands for load displacement. The strength degradation coefficient of the joints basically remained between 0.97 and 1.01 before failure, indicating that the joints had good overall stability and seismic behavior without significant strength degradation. The strength degradation rate of specimen J-1 was higher than that of specimen J-5 without side plates in the late loading periods. Specimen J-5 showed large deformation, and its bearing capacity decreased because the CFST column was subjected to a more significant bending moment and shear force. Additionally, the joint panel zone underwent a column–hinge failure, which proved that side plates enhance the seismic behavior of the joints. The specimens J-2 and J-3 failed during the tensile process, and their strength degraded drastically. Further, increasing the length of the side plates raised the strength of the specimens, but they still deformed

significantly in the late loading period. The strength degradation of the specimen J-4 in the initial period was similar to that of specimen J-1 and slowed in the late loading period. However, specimen J-4 underwent strength degradation earlier than the specimen J-1. From the failure of specimen J-4, it can be inferred that its core concrete failed due to the lack of the constraint of the binding bars on its joint panel zone, resulting in the early strength degradation of its joint. Specimens J-6 and J-7 showed less strength degradation compared to the specimen J-1 at the same horizontal displacement. Moreover, the degradation rate of strength in the specimens occurred later and was slowed down, indicating that joints with large axial compression ratios have better seismic behavior.

4.6. Energy Dissipation. The equivalent viscous damping coefficient (h_e) is one of the critical indicators of measuring

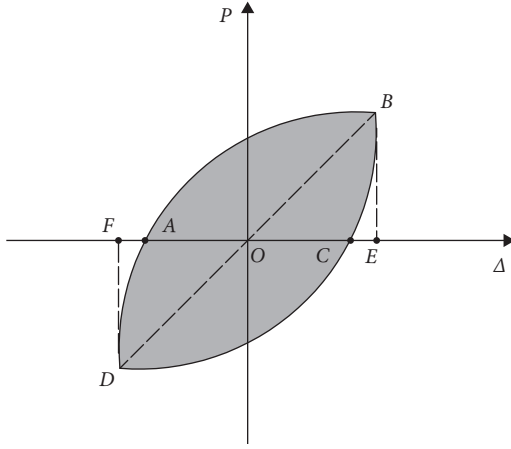


FIGURE 18: Energy dissipation calculation diagram.

TABLE 5: The equivalent viscous damping coefficient.

Specimen	J-1	J-2	J-3	J-4	J-5	J-6	J-7
h_e	0.147	0.153	0.234	0.164	0.141	0.173	0.226

the energy dissipation of structures, as seen in Figure 18. The area of the hysteresis curve (S) refers to the amount of energy dissipation, and Equation (4) can define h_e as follows:

$$h_e = \frac{(S_{ABC} + S_{CDA})}{2\pi(S_{OBE} + S_{ODF})}, \quad (4)$$

where S is the area enclosed by curve as shown in Figure 18.

Table 5 presents h_e of all the specimens. The h_e of all the specimens ranged from 0.141 to 0.234, significantly higher than that of shaped reinforced concrete columns with an h_e of 0.1. The energy dissipation of the joints with side plates satisfies seismic design requirements and is superior to that of reinforced concrete structures. The h_e of specimens J-1, J-2, J-3, J-4, J-6, and J-7 was found to be higher than that of J-5, indicating that the proposed joint configurations can enhance the energy dissipation capacity of the structure and improve its seismic behavior. Furthermore, the energy dissipation capacity was found to be significantly affected by the side plate length and axial compression ratio. Specifically, the energy dissipation capacity of the specimen increased with the increase of the side plate length and axial compression ratio.

5. Conclusions

This paper designed a structure form of the joint with side plates. A comparative analysis was conducted between the low-cycle reciprocating load test results and the design parameters of the joint, including the presence of side plates, side plate length, the presence of binding bars, and axial compression ratio. The study focused on the seismic performance, force transmission path, and the rationality of joint design. Conclusions can be drawn from the findings as follows:

- (1) The failure modes of the joints with side plates were consistent, and the failure mainly concentrated on the upper and lower flange of steel beam, with no significant damage observed to the CFST column or joint panel zone. The bearing capacity of panel zone was strengthened by the action of the side plate, and part of the bending moment was transferred to the steel beam. Such joints were in accordance with the “beam–hinge damage” mode and met the seismic design requirements of “strong column and weak beam, strong joint and weak member.” The joint without side plates was failed in the core area of column, and the plastic hinge was formed at the column end, which belonged to the “column–hinge damage” mode.
- (2) The load–displacement hysteresis curves of the six joints connected by side plates all had a relatively full shape, and there were no apparent pinch phenomena. The ultimate bearing capacity was sufficient, the strength degradation was little noticeable, and the deformation capacity was strong quite in the later experimental stage, indicating good seismic behavior.
- (3) Although binding bars did not significantly improve the bearing capacity of the T-shaped CFST column–steel beam joints, the lack of the confinement of the binding bars on the joint panel zone led to the early strength degradation of the joints, reduced the stiffness and ductility of the components, and ultimately gave rise to the poor seismic behavior of the joints.
- (4) Appropriately raising the length of the side plates improved the energy dissipation capacity and ductility of the joints to a certain extent, but the effect of delaying the degradation of strength and stiffness was not as obvious as changing the axial compression ratio. With the increase of axial compression ratio, the ultimate bearing capacity, energy dissipation capacity, and ductility of the specimens increased. At the later stage of loading, the strength degradation rate decreased and the stiffness degradation rate increased when the axial compression ratio was large.

Data Availability

The datasets analyzed during the current study are available from the corresponding author on reasonable request.

Conflicts of Interest

The authors declare that there is no conflict of interest regarding the publication of this paper.

Acknowledgments

This paper was funded by the Key Scientific Research Project of Higher Education of Henan Province, China (grant no. 22B560023), the Key Scientific Research Project Plan of

Colleges and Universities in Henan Province, China (grant no. 20zx009).

References

- [1] S. Yan, G. Kang, and Y. Wang, *Comprehension and Application of Technical Specification for Concrete Structures with Special-Shaped Columns*, China Architecture & Building Press, Beijing, China, 2007.
- [2] Ministry of Housing and Urban-Rural Development of the People's Republic of China, *Technical Specification for Concrete Structures with Specially Shaped Columns; JGJ 149-2017*, China Architecture & Building Press, Beijing, China, 2017.
- [3] H. Li, Y. Tong, J. Yin, H. Zhang, and C. Yan, "Study on axial compression behavior of cross-shaped and L-shaped multi-cavity concrete-filled steel tube special shaped column," *International Journal of Steel Structures*, vol. 22, no. 1, pp. 153–175, 2022.
- [4] Y. Yang, H. Yang, and S. Zhang, "Compressive behavior of T-shaped concrete filled steel tubular columns," *International Journal of Steel Structures*, vol. 10, no. 4, pp. 419–430, 2010.
- [5] Y. Zheng, W. Liang, S. Ma, and S. Zeng, "Behavior of stiffened and multi-cell L-shaped CFST columns under eccentric compression," *Thin-Walled Structures*, vol. 174, Article ID 109156, 2022.
- [6] J. Liu, Y. Yang, H. Song, and Y. Wang, "Numerical analysis on seismic behaviors of T-shaped concrete-filled steel tubular columns with reinforcement stiffeners," *Advances in Structural Engineering*, vol. 21, no. 9, pp. 1273–1287, 2018.
- [7] X. Liu, C. Xu, J. Liu, and Y. Yang, "Research on special-shaped concrete-filled steel tubular columns under axial compression," *Journal of Constructional Steel Research*, vol. 147, pp. 203–223, 2018.
- [8] Z.-L. Zuo, J. Cai, Q.-J. Chen, X.-P. Liu, C. Yang, and T.-W. Mo, "Performance of T-shaped CFST stub columns with binding bars under axial compression," *Thin-Walled Structures*, vol. 129, pp. 183–196, 2018.
- [9] P. Xu, Z. Wang, B. Mou, and D. Gao, "Seismic performance of CFST column to steel beam joint with outer annular stiffener," *Journal of Building Engineering*, vol. 54, Article ID 104679, 2022.
- [10] Q. Ye, Y. Wang, Z. Wang, Y. Lin, C. Shu, and F. Zhang, "Experimental study of through diaphragm bolted joint between H-beam to CFST column," *Journal of Constructional Steel Research*, vol. 182, Article ID 106647, 2021.
- [11] E.-F. Deng, Y.-H. Wang, Z. Liu, Y.-J. Song, Z. Wang, and D.-B. Cao, "Experimental study and numerical simulation for the seismic performance of an innovative connection between a flat CFST column and an H beam," *Buildings*, vol. 12, no. 6, Article ID 735, 2022.
- [12] H. Li, J. Xue, X. Chen, G. Tu, X. Lu, and R. Zhong, "Experimental research on seismic damage of cross-shaped CFST column to steel beam joints," *Engineering Structures*, vol. 256, Article ID 113901, 2022.
- [13] J. Xue, H. Li, X. Chen, X. Lu, G. Tu, and R. Zhong, "Experimental research on seismic damage of T-shaped CFST column to steel beam joints," *Structures*, vol. 38, pp. 1380–1396, 2022.
- [14] J. Zhang, Y. Li, Y. Zheng, and Z. Wang, "Seismic damage investigation of spatial frames with steel beams connected to L-shaped concrete-filled steel tubular (CFST) columns," *Applied Sciences*, vol. 8, no. 10, Article ID 1713, 2018.
- [15] G. F. Du, C. Ma, and C. X. Xu, "Experimental research on seismic behavior of exterior frame joints with T-Shaped CFST column and steel beam," *Advanced Materials Research*, vol. 368–373, pp. 183–188, 2011.
- [16] X. Tang, Y. Yang, W. Yang, J. Lanning, and Y. F. Chen, "Experimental and numerical investigation on the seismic behavior of plane frames with special-shaped concrete-filled steel tubular columns," *Journal of Building Engineering*, vol. 35, Article ID 102070, 2021.
- [17] W. Zhang, Z. Chen, Q. Xiong, T. Zhou, X. Rong, and Y. Du, "Experimental seismic behaviour of L-CFST column to H-beam connections," *Steel and Composite Structures*, vol. 26, no. 6, pp. 793–808, 2018.
- [18] Y. Cheng, Y. Yang, B. Li, J. Liu, and Y. F. Chen, "Mechanical behavior of T-shaped CFST column to steel beam joint," *Journal of Constructional Steel Research*, vol. 187, Article ID 106774, 2021.
- [19] Q. Xiong, W. Zhang, Z. Chen, Y. Du, and T. Zhou, "Experimental study of the shear capacity of steel beam-to-L-CFST column connections," *International Journal of Steel Structures*, vol. 19, no. 3, pp. 704–718, 2019.
- [20] Y. Yang, W. Yang, X. Tang, and Y. Cheng, "Seismic behavior of plane frame with special-shaped CFST columns, H-shaped steel beams and vertical rib connections," *Structures*, vol. 31, pp. 721–739, 2021.
- [21] T. Zhou, Y. Jia, M. Xu, X. Wang, and Z. Chen, "Experimental study on the seismic performance of L-shaped column composed of concrete-filled steel tubes frame structures," *Journal of Constructional Steel Research*, vol. 114, pp. 77–88, 2015.
- [22] W. Zhang, S. Jia, Q. Xiong et al., "Investigation of side plate connections in an S-CFST column frame under a column-loss scenario," *Structures*, vol. 32, pp. 1302–1319, 2021.
- [23] J. Liu, Y. Yang, J. Liu, and X. Zhou, "Experimental investigation of special-shaped concrete-filled steel tubular column to steel beam connections under cyclic loading," *Engineering Structures*, vol. 151, pp. 68–84, 2017.
- [24] Y. Cheng, Y. Yang, B. Li, and J. Liu, "Research on seismic behavior of special-shaped CFST column to H-section steel beam joint," *Advances in Structural Engineering*, vol. 24, no. 13, pp. 2870–2884, 2021.
- [25] B. Li, Y. Yang, J. Liu, X. Liu, Y. Cheng, and Y. F. Chen, "Behavior of T-shaped CFST column to steel beam connection with U-shaped diaphragm," *Journal of Building Engineering*, vol. 43, Article ID 102518, 2021.
- [26] Y. Zhao, F. Li, M. Yan, and Q. Li, "Flexural capacity of cross-shaped concrete-filled steel tubular column–steel beam joints with side-plate connections," *Sustainability*, vol. 15, no. 1, Article ID 541, 2023.
- [27] H. Chen, L. Wu, H. Jiang, and Y. Liu, "Seismic performance of prefabricated middle frame composed of special-shaped columns with built-in lattice concrete-filled circular steel pipes," *Structures*, vol. 34, pp. 1443–1457, 2021.
- [28] *Metallic Materials—Tensile Testing—Part 1: Method of Test at Room Temperature*, Standards Press of China, Beijing, China, GB/T 228.1-2010, 2010.
- [29] *Standard for Test Methods of Concrete Physical and Mechanical Properties*, China Architecture & Building Press, Beijing, China, GB/T 50081-2019, 2019.
- [30] *Specification for Seismic Test of Buildings*, China Architecture & Building Press, Beijing, China, JGJ/T 101-2015, 2015.
- [31] Y. Tang, Y. Wang, D. Wu et al., "An experimental investigation and machine learning-based prediction for seismic performance of steel tubular column filled with recycled aggregate concrete," *Reviews on Advanced Materials Science*, vol. 61, no. 1, pp. 849–872, 2022.
- [32] Y. Tang, M. Zhu, Z. Chen et al., "Seismic performance evaluation of recycled aggregate concrete-filled steel tubular

columns with field strain detected via a novel mark-free vision method,” *Structures*, vol. 37, pp. 426–441, 2022.

- [33] Z. He, S. Hu, B. Li, Y. Yang, and Y. Cheng, “Research on seismic behavior of cruciform special-shaped CFST column to H-section steel beam joint,” *Journal of Building Structures*, vol. 43, pp. 95–106, 2022.
- [34] *Technical Specification for Structures with Concrete-Filled Rectangular Steel Tube Members*, China Planning Press, Beijing, China, CECS 159: 2004, 2004.